Boundary-Layer Meteorol (2010) 135:209–228
DOI 10.1007/s10546-010-9477-0

ARTICLE

Organized Structure of Active Turbulence Over an Array of Cubes within the Logarithmic Layer of Atmospheric Flow

Atsushi Inagaki · Manabu Kanda

Received: 17 August 2009 / Accepted: 12 February 2010 / Published online: 4 March 2010

Abstract We investigate the coherent structure of atmosphere turbulence over very large roughness within a fully rough, high Reynolds number turbulent flow. The horizontal distributions of coherent turbulence were determined by multipoint measurements of velocity fluctuations using sonic anemometers in a comprehensive outdoor scale model experiment for urban climate (COSMO). COSMO is made up of 512 cubical obstacles, each 1.5 m on a side, arranged in a rectangular pattern on a flat 50 m × 100 m concrete plate. A total of 15 sets of sonic anemometers were aligned horizontally within the logarithmic layer above this site. The velocity fluctuations observed in COSMO were decomposed into active and inactive contributions by applying a spatial-filtering method, and which used a simple moving average along the spanwise direction of the predominant flow as a filter function. The size of the filter should be between the sizes of the active and inactive fluctuations. This method potentially eliminates the considerable portion of low frequency modes included in the horizontal velocity fluctuation, while preserving well the Reynolds stress. The structural characteristics of the active turbulence were qualitatively similar to those measured over various surface configurations. Overall, the observed structures of the active turbulence are composed of very large streaks of low momentum fluid elongated in the streamwise direction with some sub-structures included in the streaks. The sub-structures were the main cause of the ejections, which accompany horizontal vortices. The active motion, including the streaky structures, did not reproduce the lower frequency peak of the bi-modal distribution of the horizontal velocity spectra, but reproduced the higher frequency mode that robustly follows inner-layer similarity (i.e. Monin–Obukhov similarity).

A. Inagaki (✉)
Department of Civil Engineering, Tokyo Institute of Technology, Tokyo, Japan
e-mail: inagaki.a.ab@m.titech.ac.jp

M. Kanda
Department of International Development Engineering, Tokyo Institute of Technology, Tokyo, Japan

Keywords Active motion · Atmospheric turbulence · Coherent structure of turbulence · Low speed streaks · Monin–Obukhov similarity · Reduced urban scale model

1 Introduction

We investigate the coherent structure of turbulence within a logarithmic region of a fully rough boundary layer over an array of cubic obstacles. The study of coherent turbulence has usually been motivated by understanding the physical background of the statistical structure of wall turbulence, or by modelling or controlling it for industrial or geophysical applications (Robinson 1991). Although our motivation is based on the geophysical application of the understanding of the turbulent exchange process of momentum and scalars in the near-surface region, it includes points of general interest in fluid mechanics concerning fully rough turbulent flow, the effects of roughness, and that of inactive turbulence.

Townsend (1976) developed a set of hypotheses concerning wall turbulence (reviewed by Raupach et al. 1991), which declared that boundary-layer turbulence is composed of active and inactive eddies. Active eddies are responsible for vertical momentum transfer, while inactive eddies are not. Based on Townsend's Reynolds number similarity for turbulent flow, the structure of active eddies is geometrically similar for any geometrical surface and all Reynolds numbers that are large enough to allow fully turbulent flow.

This similarity hypothesis has been evaluated in many studies with respect to integrated statistics, some of which support the statistical similarity (e.g., Raupach et al. 1991; Inagaki and Kanda 2008) and others that contradict it (e.g., Krogstad et al. 1992; Bhaganagar et al. 2004). In contrast with the numerous statistical investigations, there are few studies pertaining to the structural or dynamical similarity of coherent eddies in the logarithmic region of a fully rough boundary layer (e.g., Hutchins and Marusic 2007; Volino et al. 2007).

Studies of the coherent structure of wall turbulence have often been conducted using a flat wall in laboratory and numerical experiments. Some studies have addressed packets of hairpin vortices for the outer-layer structure (e.g., Head and Bandyopadhyay 1981; Adrian et al. 2000; Tomkins and Adrian 2003). Adrian et al. (2000) proposed a conceptual model of a turbulent structure composed of a group of hairpin vortices that align in the streamwise direction and form a streaky structure of low momentum. This elongated structure is much larger than that found in the near-surface region, which has an almost constant span of 100 viscous lengths (Klein et al. 1967).

In contrast, much less is known about the structure of coherent turbulence over very rough surfaces. The effects of massive roughness on coherent turbulence within the logarithmic layer are still under investigation. Many studies have used numerical simulations based on large-eddy simulation (LES) or direct numerical simulation (DNS) to provide insight into the three-dimensional (3D) nature of coherent turbulence, although these studies have significant limitations in the computational domain size or resolution. LES has been used to simulate fully rough turbulent flows over an array of cubes that are explicitly resolved (e.g. Kanda et al. 2004; Kanda 2006), over vegetation (e.g. Watanabe 2004), and geographical flows over modelled rough surfaces (e.g. Foster et al. 2006). Even though the surface conditions are different in each simulation, all of them contain very large-scale streaks of low momentum fluid in their inertial sublayers. DNS has also been used to investigate turbulent flow over massive roughness with low or moderate Reynolds numbers. These studies also revealed streaky structures (Bhaganagar et al. 2004) and hairpin vortices developed from cubical obstacles (Coceal et al. 2007).

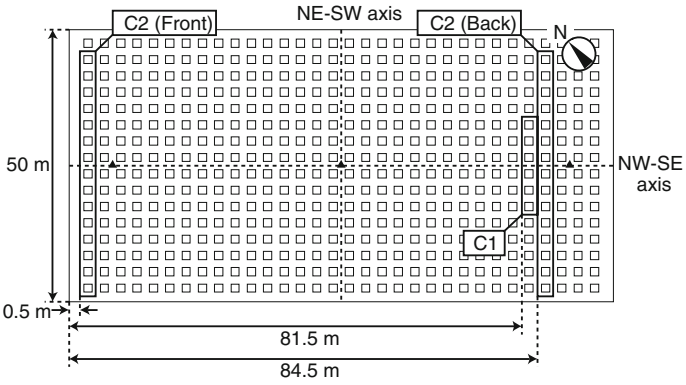

Fig. 1 Schematic of experiment COSMO. C1 and C2 indicate the locations of the instruments for the respective measurements

Several laboratory experiments have investigated the spatial distribution of turbulence for flow with very high Reynolds number over modelled vegetation (e.g. Shaw et al. 1995) and an array of cubes (e.g. Castro et al. 2006), although the size of the roughness and the scale of the motion are limited by the experimental domain size. Their spatial correlation analysis predicted the existence of an elongated structure of streamwise velocity fluctuations over very rough surfaces.

The atmosphere is another option for investigating rough wall turbulence (e.g., Kunkel and Marusic 2006; Hutchins and Marusic 2007), where the Reynolds number is usually very high and the geophysical surfaces are very rough (e.g., forests and cities). There are many experiments of atmospheric turbulence within the surface layer over very rough surfaces that have focused on turbulent structures, e.g., Shaw et al. (1983) over vegetation, and Oikawa and Meng (1995), Moriwaki and Kanda (2006), and Christen et al. (2007) over cities. These experiments have usually been limited to exploring the vertical one-dimensional extent of turbulent motion, and little information is available about the horizontal extent since this requires several masts or towers horizontally distributed in the cities and forests.

In our study, we also consider atmospheric turbulence to investigate the coherent motion within very rough flow over massive urban roughness. The investigation was conducted in a comprehensive outdoor scale model experiment for urban climate (COSMO, Fig. 1), which is characterized by large roughness, a fully rough Reynolds number, and no upper boundary. Detailed descriptions of COSMO can be found in Kanda et al. (2007) and Inagaki and Kanda (2008).

While this experiment provides a unique dataset with respect to the Reynolds number and size of roughness, the use of atmospheric flow, compared to artificial flows, introduces several uncertainties attributed to synoptic variations. However, the integrated statistics and spectra of turbulent fluctuations in COSMO maintain the similarity of inner-layer scaling quite well (Inagaki and Kanda 2008), and so the COSMO experiment is useful for examining the nature of wall turbulence accounting for the similarity law. The objective of this study is to observe experimentally the coherent structures of active turbulence, in particular focusing on their horizontal distribution over very large roughness for flow with high Reynolds number.

In the following, we denote the streamwise, spanwise, and wall-normal coordinates in the form (x, y, z), and the wind-speed components of the respective wind directions as (u, v, w). The temperature is denoted as θ.

2 Theoretical Background

The method to separate the active and inactive motions is now described. The term 'active' is generally used to refer to the direct contribution to the turbulent momentum transport or Reynolds stress generation (Townsend 1976). Here we use the term 'active motion', in a broader sense, as a sequence of turbulent motions that reproduces the inner-layer similarity (also proposed by Townsend), such as the coherent structures composing the regeneration cycle of turbulent flow (Kawahara and Kida 2001) and the sequence of very large-scale motion (VLSM, Kim and Adrian 1999).

2.1 Scale Decomposition of Natural Turbulence

Townsend (1976) expected that the size of inactive motions is sufficiently larger than that of active motions and that they scarcely interact with each other. Based on this assumption, we accomplished the separation of active and inactive motions by using a filtering method that separates the natural fluctuations into different scales. The practical application of the decomposition of natural turbulence has been discussed by McNaughton and Raubach (1998) and Lewalle et al. (2000).

Turbulent fluctuations are usually defined as the residuals from the temporal average if the data are based on a single-point measurement,

$$\varphi = \overline{\varphi} + \varphi', \tag{1}$$

where φ is a physical variable such as the velocity component or temperature. The overbar and the prime indicate the temporal mean and fluctuation terms, respectively; this definition of fluctuation generally involves several time scales of motions that are smaller than the averaging time.

For another definition of the fluctuation, the natural fluctuation is filtered using a simple moving average in space or time to separate high and low frequency motions as,

$$\varphi = [\varphi]_m + \varphi'_m, \tag{2}$$

where the square brackets and prime with subscript m indicate the moving averaged component and the residual fluctuation component, respectively. If the size of the filter, Δ, which is equal to the range for a moving average, is sufficiently larger than the size of the active turbulence, while sufficiently smaller than the size of the inactive motions, then the active and inactive motions can approximately be separated as in Eq. 2.

Since the temporal mean of φ'_m is not guaranteed to be zero due to the finite averaging area and the internal variation of external fluctuations, a temporal average is further applied to φ'_m to define the local temporal fluctuation,

$$\varphi = [\varphi]_m + \overline{\varphi'_m} + \varphi''. \tag{3}$$

The double prime indicates the fluctuation component that was filtered using a moving average, and approximates the active motion under the ideal situation explained above.

2.2 Application of the Scale Decomposition of Atmospheric Turbulence in COSMO

The separation of active and inactive motions is accomplished for the measurements in COSMO by using a simple moving average as a filter function. The filtering is applied to the

spatial variation in the spanwise direction since this distribution is directly observed in this experiment. For comparison, we also tried the moving average in time, which is assumed to be in the streamwise direction based on Taylor's frozen turbulence hypothesis. The difference of the filtering directions distinguishes the spanwise and streamwise length scales of turbulent motions to be decomposed.

The application of Eq. 3 to the experimental datasets in COSMO requires a reasonable determination of the filter size, Δ, for separating the active and inactive motions. In this study, Δ is defined as the distance between a reference point and the furthest point of the averaging area of the moving average.

The filter size, Δ, should be a scaling between the sizes of the active and inactive fluctuations. Although the theoretical derivation of Δ is difficult, the rough empirical estimation of relevant turbulent scales is possible. The size of inactive motion can be related to the atmospheric boundary-layer (ABL) height ($\approx$1 km), whereas the size of active turbulence can be related to the size of the roughness element. COSMO has smaller sized cubes than actual buildings in the real world. Therefore, the scale gap between the inactive and active motions in COSMO is expected to be sufficiently larger than the real urban boundary layer. The larger scale gap makes the separation process easier and clearer.

3 Experimental Set-up

3.1 COSMO

Detailed descriptions of COSMO can be found in Kanda et al. (2007) and Inagaki and Kanda (2008) but, in brief, the COSMO experimental facility was constructed at the Nippon Institute of Technology in Saitama, Japan. There are 512 concrete cubes and three 8-m tall meteorological towers on a flat concrete plate. The cubes, which are 1.5 m($= H$) on a side, are arranged regularly as shown in Fig. 1. The axis parallel to the street along the longer side of COSMO is named the 'NW–SE' axis, and the axis perpendicular to it is named the 'NE–SW' axis. The mean wind direction was usually from the north-west during the experiments.

The mean flow characteristics for COSMO are also described in Inagaki and Kanda (2008). In general, at the height of $2H$, the mean flow statistics are horizontally homogeneous, and independent of the individual roughness cubes. The Reynolds stress is nearly constant with height, and the mean velocity changes logarithmically in the vertical direction around $2H$. Therefore, a measurement of the horizontal distribution of the turbulence was conducted at $2H$ where the logarithmic region develops.

3.2 Instrumentation

Spatial distributions of the velocity fluctuations were deduced from multipoint measurements using sonic anemometers. Two types of sonic anemometers were used: 10 sets of Kaijo DA600 (TR90AH), and 30 sets of Young Model 81000. The DA600 (TR90AH) anemometer can measure 3D velocities and temperature at 50 Hz, while the Model 81000 anemometer can capture the same measurements at 30 Hz. A comparison of both types of instruments that was conducted on site showed that the Model 81000 anemometer had a tendency to underestimate the vertical velocity fluctuations in this experiment; however, measurements of the horizontal velocity fluctuations were almost the same for both devices.

3.3 Instrument Settings

The sonic anemometers were aligned horizontally at a constant height above the ground. The velocity and temperature fluctuations were measured synchronously at each location. When the horizontal mean flow crosses this line, we obtained a horizontal two-dimensional distribution of the velocity and temperature fluctuations by assuming Taylor's frozen turbulence hypothesis in the streamwise direction, and by direct measurement in the spanwise direction (e.g. Lewalle et al. 2000; Porté-Agel et al. 2001; Hutchins and Marusic 2007). Based on this strategy, we used the following two instrument configurations. The horizontal locations of these settings are seen in Fig. 1.

In configuration 'C1', the 10 sets of DA600 (TR-90AH) anemometers were aligned horizontally parallel to the NE–SW axis at a constant height of 3.0 m from the ground and 84.5 m from the north-west edge of COSMO (Figs. 1, 2a). The probe heads of the anemometers were directed north-west to capture the flow from that direction. The measurement points were spaced at a uniform 1.5-m distance. Therefore, the horizontal distribution of the measurement points ranged up to 13.5 m in the spanwise direction. The datasets were collected synchronously at 50 Hz using a TEAC LX10 data logger system. This configuration was designed to measure the horizontal distribution of the turbulent fluctuations, and evaluate the method of separating the active and inactive turbulence, since these anemometers can measure reliably the vertical velocity fluctuations and Reynolds stress. The measurements were conducted continuously for 39 days from May 28, 2007 to July 5, 2007.

The second configuration, 'C2', was designed mainly to capture the horizontal distribution of the turbulent fluctuations over a wider horizontal range than C1. For this reason, we used the Model 81000 anemometers to increase the number of measurement points. Two sets of 15 Model 81000 devices were placed in 42-m straight lines along the NE–SW axis at the

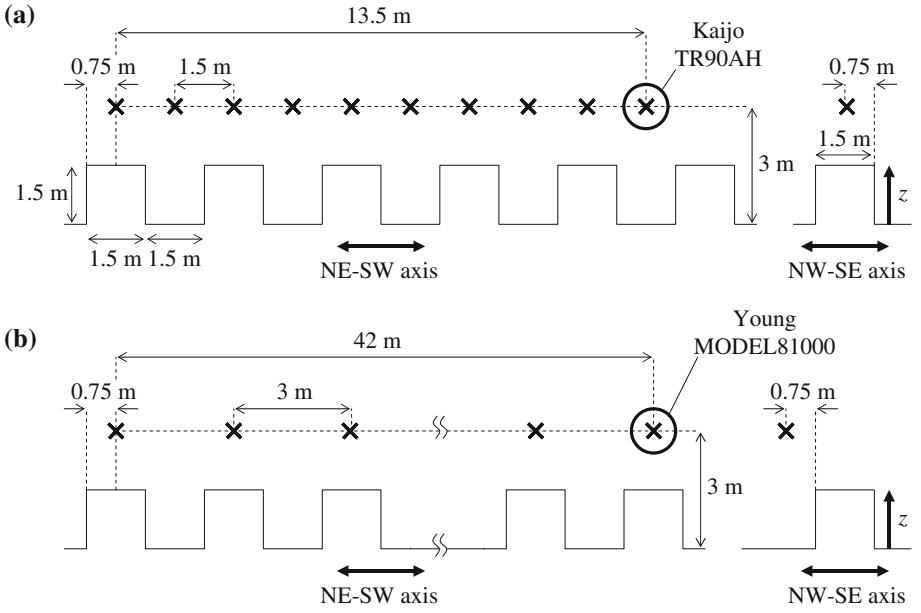

Fig. 2 Configurations of the measurement probes for, (**a**) setting C1, and (**b**) C2 of the front or back sides of COSMO

upwind and downwind sides of COSMO (Fig. 2b). The instruments were spaced at uniform 3-m intervals. The upwind and downwind rows were 84 m apart. All measured parameters, i.e., 30 sets of 3D velocity and temperature data, were collected at a sampling rate of 10 Hz using a CHINO KE3000 data logger system. Although this sampling rate might not be sufficient to investigate fine-scale eddies, it is useful for examining very large-scale motions. The measurements were conducted for 3 months, from November 9, 2006 to January 30, 2007. There was no overlap with the period used for C1.

3.4 Data Acquisition and Qualification

We used the same averaging procedure and data qualification to derive both the mean statistics and the instantaneous turbulent structures so they could be directly compared.

The averaging time was selected to be 30 min to obtain reliable statistics in the atmospheric boundary layer (Stull 1988). We only analysed the flows from a direction nearly perpendicular to the row of anemometers so as to obtain the turbulent fluctuations on a horizontal plane as wide as possible in the spanwise direction. The acceptable deviation of the mean wind direction was less than 5° from the NW–SE axis. For the analysis, we selected datasets whose mean wind speed was greater than 1.0 m s^{-1} at the height $2H$ to avoid extremely low speed periods. The roughness Reynolds number Re^* ($= z'u_*/\nu$) was 10^4–10^5, where z' is the effective height (m) defined as the difference between the actual height z and the displacement height d(m), and u_* is the friction velocity (ms^{-1}).

Since buoyancy effects are beyond the scope of our study, only near-neutrally stratified flow was analysed. The near-neutral stratification was confirmed using the atmospheric stability parameter,

$$\frac{z'}{L} = -\frac{(g/\overline{\theta})(\overline{w'\theta'})kz'}{u_*^3}, \tag{4}$$

where L is the Obukhov length (m), g is the acceleration due to gravity (m s^{-2}), and k is the von Karman constant, taken as 0.4. The acceptable range of the atmospheric stability parameter was $|z'/L| < 0.05$ based on the results of Inagaki and Kanda (2008).

4 Spectral Characteristics of Active Turbulence

In this section, we investigate the spectral characteristics of active turbulence estimated using two kinds of filter; one uses the moving average in the spanwise direction, and another uses similar in the temporal domain. The datasets obtained at the south-west side in setting C1 (see Fig. 2a) were used in this investigation since the size of the filter Δ in the spanwise direction ranges from H to $9H$. Any statistical values shown are the ensemble averages of the 30- min mean values obtained from selected time intervals.

4.1 Applicability of the Filter in Space

Figure 3 shows the ensemble averages of the turbulent velocity spectra (S_u, S_v, S_w) and the Reynolds stress cospectra (Co_{uw}) derived from unfiltered and filtered fluctuations in the spanwise direction for different sizes of Δ. These spectra were calculated using fast Fourier transforms; frequency was converted to wavenumber ($f/\overline{u}$) assuming the frozen turbulence hypothesis. The spectral densities and wavenumbers were normalized by the inner-layer

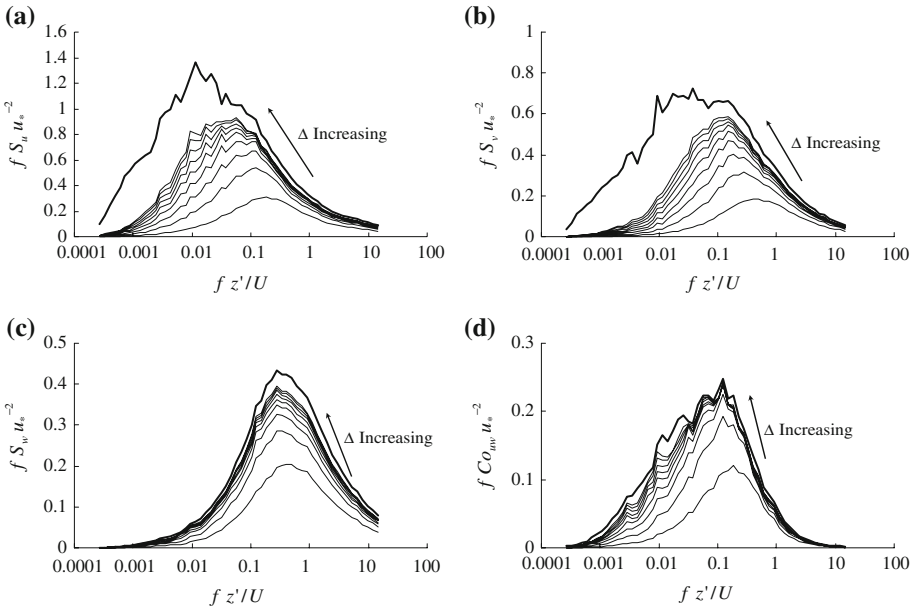

Fig. 3 Pre-multiplied spectra and cospectra for unfiltered (*bold line*) and filtered fields in the spanwise direction. The spectra and cospectra are normalized by u_*, plotted on log-linear axes: (**a**) streamwise velocity spectra, (**b**) spanwise velocity spectra, (**c**) wall-normal velocity spectra, and (**d**) cospectra of the Reynolds shear stress. The size of filter Δ ranges from H to $9H$

variables u_* and z', respectively. The value of u_* is estimated from the root mean of $-\overline{u'w'}$ at $2H$, which is the unfiltered variable. The shapes of these spectra of the unfiltered fluctuation agree well with those of Kaimal et al. (1972), except for the low frequency parts of the u and v spectra (not shown), as observed in many atmospheric field experiments.

For all spectra and cospectra, the spectral densities filtered in the spanwise direction become smaller than the unfiltered values for the range of Δ in the current analysis. Specifically, the spectral densities at the lower frequencies were effectively reduced by the filtering, although they are not reduced to zero. With increasing Δ in the spanwise direction, their spectral densities increased and approximated the values of the unfiltered spectra. When the size of the filter is $9H$, the total shapes of the filtered w spectra and uw cospectra were almost consistent with those of the unfiltered spectra. Meanwhile, the filtered u and v spectra for the lower frequency range still have a considerable deficit relative to their unfiltered values. This implies that the low frequency motion, which is included in the horizontal velocity fluctuation and filtered in the spanwise direction, was nearly 'inactive' to the Reynolds stress.

Figure 4 shows the integrated contribution of the turbulent intensity and Reynolds stress filtered in the spanwise direction (i.e. $\overline{u''u''}$, $\overline{v''v''}$, $\overline{w'w'}$, and $\overline{u''w''}$) on the unfiltered values (i.e. $\overline{u'u'}$, $\overline{v'v'}$, $\overline{w'w'}$, and $\overline{u'w'}$, respectively). When $\Delta = 9H$, the filtered u and v fluctuations accounted for only 50–60% of the unfiltered turbulent intensities. Meanwhile, the filtered uw covariance accounted for more than 90% of the unfiltered value.

Kim and Adrian (1999) suggested that the u spectra are composed of a bimodal distribution whose components are roughly distinguished by low and high frequency modes. Although the second peak of the u spectra is ambiguous, these two modes can be distinguished by the inflection of the spectral curve. The low frequency mode can be scaled with outer-layer

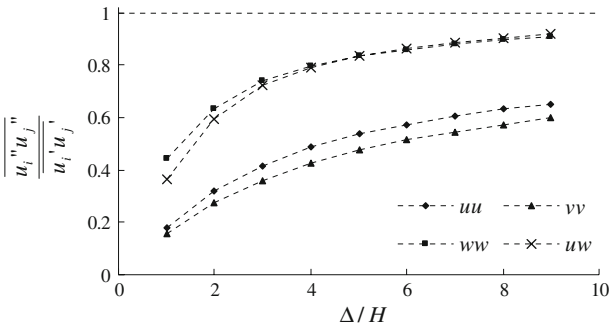

Fig. 4 Ratio of the turbulent intensity filtered in the spanwise direction and unfiltered turbulent intensities for different sizes of filter

variables such as the boundary-layer height δ, and the high frequency mode can be scaled with inner-layer variables such as z. Nickels et al. (2005) demonstrated that such a bimodal distribution of the u spectra can be scaled with a ratio of inner- and outer-layer variables, such as z/δ.

Similar bimodal distributions of the u spectra have also been observed in atmospheric field experiments (e.g. Kaimal et al. 1972; Kunkel and Marusic 2006; Inagaki and Kanda 2008). Kunkel and Marusic (2006) indicated that high frequency and low frequency modes of the atmospheric turbulence can also be scaled with inner- and outer-layer variables. In this case, the outer-layer variable is usually represented by the ABL depth z_i (e.g. Kaimal et al. 1972).

The unfiltered u spectra in COSMO also have a similar bimodal distribution in Kim and Adrian (1999), whose peak frequencies are roughly estimated at 0.01 and 0.1. These two modes were clearly separated using the filter in the spanwise direction; one accounts for the high frequency mode that satisfies the $-5/3$ power law and follows the inner-layer scaling similarity, while the other accounts for the major part of the lower frequency mode that was filtered out. Therefore, it is expected that the low frequency mode has an outer-layer length scale and is nearly inactive to the local Reynolds stress. Meanwhile, the high frequency mode has an inner-layer length scale, and is active.

4.2 Statistical Similarity of the Active Motion

It is well known that Monin–Obukhov similarity fails, at least in part, for the variables related to the horizontal velocity fluctuations. One reason is the contribution of inactive motions since these do not follow scaling by inner-layer variables. Inagaki and Kanda (2008) proposed a relation explaining the similarity of the standard deviation of the horizontal velocity fluctuation normalized by the friction velocity (σ_u/u_*, σ_v/u_*) as,

$$\left(\frac{\sigma_u}{u_*}\right)^2 = \alpha + \frac{\overline{u_{out}^2}}{u_*^2}, \tag{5}$$

where u_{out} is the inactive low-frequency motion of the horizontal velocity fluctuation, and α is a constant. Equation 5 implies that the similarity is still valid for the horizontal velocity fluctuations in the absence of inactive motions. Therefore, we examined the similarity of horizontal velocity fluctuation by filtering out inactive motions.

Table 1 Ensemble average and the deviation of σ_u/u_* and σ_v/u_* calculated from the velocity fluctuations unfiltered and filtered in spanwise direction

	Average		Deviation	
	σ_u/u_*	σ_v/u_*	σ_u/u_*	σ_v/u_*
Unfiltered	2.59	2.03	0.16	0.2
Filtered	2.10	1.58	0.06	0.07
Lower limit	2.0	1.3		

The lower limits are estimated from the various experiments in cities, flat field and COSMO

Table 1 shows the ensemble average and the standard deviation of σ_u/u_* and σ_v/u_*, in which we do not apply the filtering to u_*. The Table also includes the lower limits of the values obtained among the various experiments in city, flat field, and COSMO setting reviewed by Roth (2000) and Inagaki and Kanda (2008). It is supposed that this lower limit should occur when the contribution of the inactive motion is negligible relative to that of the active motion, as seen in Eq. 5 (Inagaki and Kanda 2008).

The ensemble averages of the filtered σ_u/u_* and σ_v/u_* become smaller than the unfiltered values as expected from the spectral results, and come close to the lower limits of the collective data for the various experiments. The scattering of filtered variables from the ensemble averages was much less than that of the unfiltered variables, and indicates that these variables were reduced to a constant value after removing the contributions of the inactive motions regardless of the experimental setting. The results imply that Monin–Obukhov similarity is still applicable for the horizontal velocity fluctuations in respect to the active motions.

4.3 Applicability of the Filter in Time

If the filtering in time can also effectively separate the active and inactive motions, it is useful because this filtering is available in the single-point measurement. The filtering in time is examined and compared with the filtering in the spanwise direction.

Figure 5 shows the unfiltered and filtered spectra in time. The sizes of filter, which are converted from the time series assuming the frozen turbulence hypothesis, ranged from $3H$ to $9H$ along the streamwise direction with a constant interval (H). A much larger size of filter ($300H$) is also applied.

When the filter is applied in the time series, the low frequency components of the spectral energy are reduced from those in the unfiltered spectra, depending on the size of filter. However, the use of filter in time sharply cuts off the spectral energy at frequencies lower than the size of the filter. This is different from the use of the filter in the spanwise direction, which results in filtered spectra wherein the low frequency region is still preserved and the low frequency edges approximate to zero.

This sharp cut-off of spectral energy is found not only in the horizontal velocity spectra but also in the vertical velocity spectrum and the Reynolds stress cospectra. To conserve the whole Reynolds stress cospectra, we adjusted the value of Δ to a relatively large value ($\Delta = 300H$). This resulted in Reynolds stress cospectra that are almost preserved; in addition, most of the low frequency part of the horizontal velocity spectra is also preserved. In this strategy, the low frequency motion, which is separated by filter in the spanwise direction, was not separated.

The different effect of the filter in the spanwise and streamwise directions implies that the coherent structures of active and inactive motions have a comparable streamwise length (or time) scale and different spanwise length scales. This is further discussed in Sect. 5.

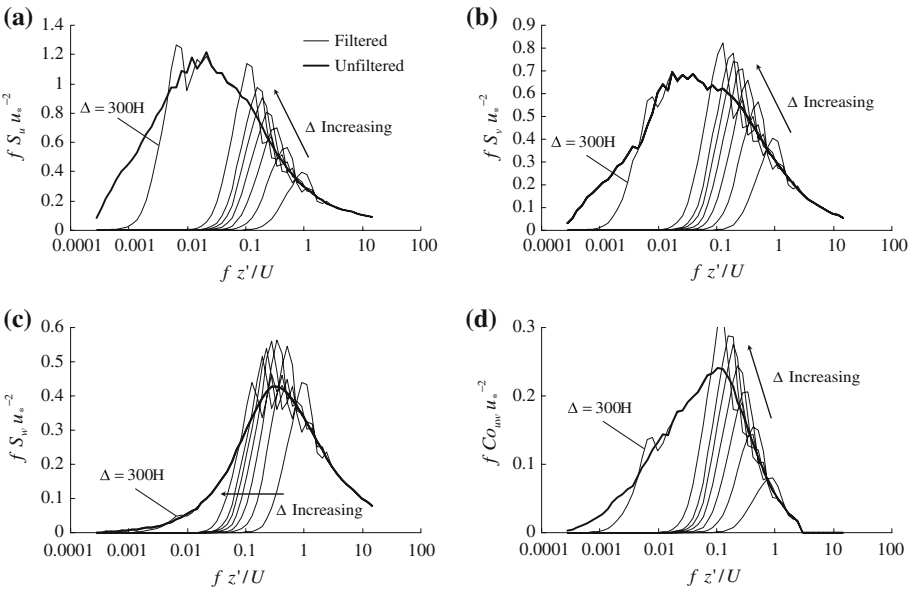

Fig. 5 Same as Fig. 3 but filtering in time. The size of filter Δ ranges from $3H$ to $9H$, and $300H$

5 Horizontal Distribution of the Active Fluctuation

We examined the horizontal distribution of the velocity fluctuation from the datasets obtained in configurations C1 and C2. In the following figures, the streamwise length scale is converted from the time scale by multiplying with the horizontal mean wind velocity, assuming the frozen turbulence hypothesis.

5.1 Horizontal Distribution of the Streamwise Velocity Fluctuations over the Entire COSMO Domain

A single 30-min dataset for the C2 configuration was extracted to visualize the horizontal distribution of u fluctuations over the entire COSMO domain. In this period, the horizontal mean wind speed at the measurement level was $5.0\,\mathrm{m\,s^{-1}}$ from the north-west, and the deviation of the mean wind direction was less than 1° from the NW–SE axis. The flow was near-neutrally stratified ($z'/L = -0.0015$). In this section, we used a singular size of filter $\Delta = 10H$ instead of $9H$, since the minimum interval of $2H$ in the spanwise direction was used for the setting C2.

Figure 6 shows the horizontal distribution of u' (unfiltered) observed at, (a) the upwind, and (b) the downwind sides of COSMO. The size of the visualized field extends 9 min in time, which is comparable to about 2700 m ($1800H$) in the streamwise direction if we assume the frozen turbulence hypothesis, and 42 m ($28H$) in the spanwise direction. The figures were folded every 3 min to maintain the aspect ratio and to facilitate visualization. It might be problematic to apply the frozen turbulence hypothesis for such a long duration in time, as reported by Dennis and Nickels (2008). However, it is true that this space-time distribution of velocity fluctuations is actually responsible for the statistical characteristics of turbulence observed

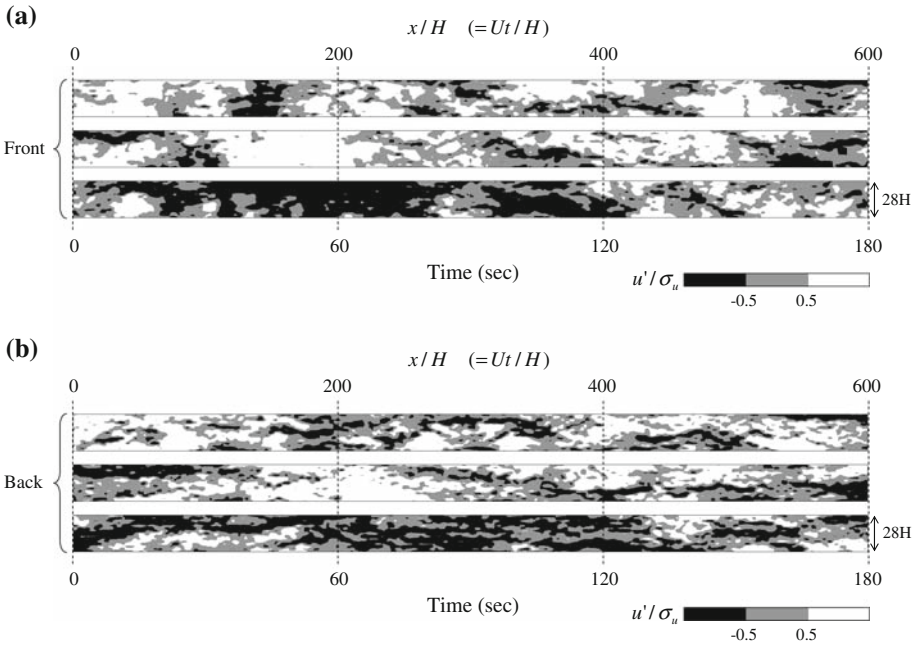

Fig. 6 Horizontal distribution of u' (unfiltered) observed at, (**a**) front, and (**b**) back of COSMO in the setting C2. The values are normalized by σ_u

for a conventional single-point location. Therefore, we use this for the direct comparison of the time-spanwise distribution of turbulence and its integrated statistics.

In Fig. 6, significant spatial heterogeneities are observed in the horizontal distribution of u' (unfiltered). These heterogeneities were not due to the direct influence of the wake turbulence from the cubes since all of the instruments were located at the same location relative to the adjacent cubes (Fig. 2b). Furthermore, Inagaki and Kanda (2008) demonstrated that the roughness sublayer, where the flow is directly influenced by roughness, is below a height of $2H$ in COSMO.

The distribution of u' (unfiltered) at the upwind side reveals some very large structures of high and low momentum fluid that cover the entire spanwise area of COSMO and exceeded a few minutes in duration. The structures on the downwind side look finer than those on the upwind side, however, they also included very large-scale variations, as observed in the upwind motion. This variation can be roughly expressed by the spatial average of u' along the spanwise direction, which corresponds to the values of the low frequency fluctuation $[u']_m$ separated by the filter in the same direction. Figure 7 shows the temporal variation of $[u']_m$ observed at the centre of the measurement arrays for the upwind and downwind sides of COSMO, which corresponds to the first 3 min of Fig. 6. For clarity, this $[u']_m$ shown in Fig. 7 is further averaged every 1 s in time. The variations of $[u']_m$ on the upwind and downwind sides agree well with a nearly constant time lag, indicating that these very large-scale variations are due to external disturbances passing through COSMO from the upwind to the downwind sides.

Next we examine the effects of filtering on the visualized flow field observed at the downwind side of COSMO. Figure 8a shows the horizontal distribution of the u fluctuation filtered in the spanwise direction (u''); the size of the filter is $10H$. The very large streaky structures

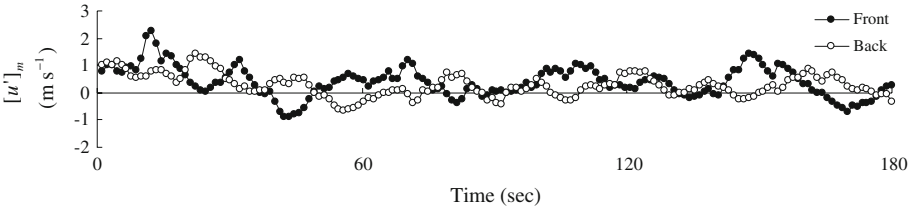

Fig. 7 Temporal variations of $[u']_m$ observed at the upwind (*filled circle*) and downwind sides (*open circle*)

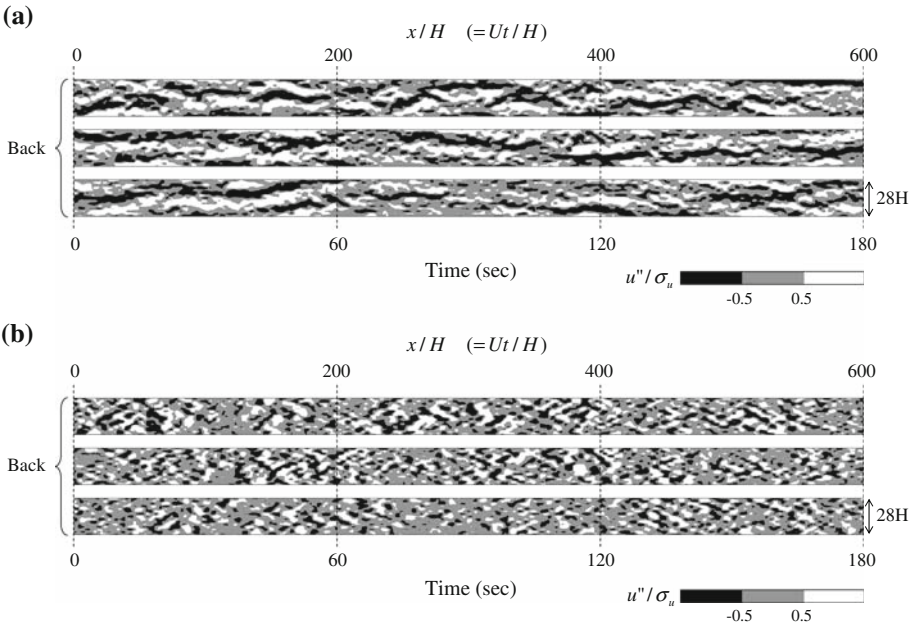

Fig. 8 Horizontal distribution of u'' (filtered) observed at the back of COSMO in the setting C2. Filtering is applied in, (**a**) spanwise direction, (**b**) time. The values are normalized by σ_u

of low momentum fluid still remain in the flow field, which was filtered in the spanwise direction.

The direct comparison of the horizontal structural characteristics and the spectral characteristics of the u fluctuations reveals that the very large streaks of the low momentum region were included in the higher frequency mode of the bimodal distribution of u spectra, which directly contributes to the major part of the Reynolds stress. This result supports the structural similarity of the streaky structure because the high frequency mode of the u spectra robustly follows inner-layer similarity (e.g. Kunkel and Marusic 2006).

For comparison, we also applied the filter in time. Figure 8b shows the horizontal distribution of the u fluctuation from the filtered fluctuation in time (u'') with the same size of filter as used in Fig. 8a ($\Delta = 10H$). The streaky structures, which were found in the unfiltered and filtered cases in the spanwise direction, were decomposed into smaller components of structures. Because the active motion is the elongated structure along the streamwise direction, the spanwise length scale of the active motion is much smaller than that of the inactive

motion. However, their streamwise length scales are comparable. Thus, the filtering in the spanwise direction effectively separates the active and inactive motions.

Similar streaky structure of the low momentum region has been observed in the logarithmic layer during various field and numerical experiments, e.g., Tomkins and Adrian (2003) and Hutchins and Marusic (2007) for flat rough surfaces in laboratory and atmospheric experiments, Watanabe (2004) and Kanda (2006) for vegetation and cubic arrays in numerical simulations. Recent single- and dual-Doppler lidar observations have also observed similar streaky structures within the atmospheric surface layer (e.g. Drobinski et al. 2004; Newsom et al. 2008). These observations qualitatively support the geometrical similarity of the streaky structure of the low momentum region within the inertial sublayer, irrespective of the surface configuration and the outer-layer motion, as hypothesized in Townsend's wall similarity hypothesis (Townsend 1976; reviewed by Raupach et al. 1991).

The quantitative examination of the geometrical similarity has also been conducted by comparing the flows over smooth and rough walls (e.g. Volino et al. 2007), and over laboratory and geophysical surfaces (e.g. Hutchins and Marusic 2007; Marsic and Hutchins 2008). They provided some evidence that similarity occurs if their spanwise length scales are normalized by the boundary-layer height, or the internal boundary-layer height for atmospheric flow.

If these structures are geometrically similar to those observed in our experiment, they are expected to be dynamically similar and behave as active motions.

5.2 Large-Scale Structures of the Low Momentum Region

The elongated structures of the low momentum region were more precisely investigated using the datasets obtained with configuration C1, in which the domain of the measurements was narrower but the spatial and temporal resolutions were finer than in configuration C2. Furthermore, it was possible to measure the w component with sufficient accuracy in configuration C1. We extracted a specific duration during which a very large streak passed through the experimental domain. Figure 9 shows the horizontal distributions of u'', w'', and $u''w''$ calculated using the filtering in the spanwise direction. The black and white parts of the distribution of $u''w''$ indicate the occurrences of the sweeps and ejections that were three times larger in magnitude than that of $-\overline{u'w'}$.

The distribution of u'' indicates a very large streak structure of low momentum fluid with horizontal meandering. Although the coherent w'' structure was finer than that of u'', both structures corresponded closely to the location where clusters of updrafts frequently occur in the very large low momentum fluid. As a result, the distribution of $u''w''$ shows that the ejections occurred discontinuously along the streak of negative u''. The wind vectors around the streak show that the spanwise velocities tend to converge into the streak, while the flow directions within the streak follow its meandering shape.

The sequence of u'' and w'' structures in COSMO agree closely with the scenario of the conceptual VLSM model developed by Kim and Adrian (1999). In that model, the VLSM was composed of several substructures of turbulence aligned in the streamwise direction. This substructure, called a 'packet structure', was also composed of several hairpin vortices (Adrian et al. 2000). These hairpin vortices entrained the surrounding air between the legs of the hairpin, which were represented by a pair of counter-rotating vortices, and ejected the air backwards and upward. Therefore, the substructures were relevant to the ejection.

Although the low speed streaks are assumed to be a passive structure driven by the substructure in the VLSM model, the streaks can be interpreted as active motions in the context of this study. This is because the flow field, including the streaks, tends to follow the inner-layer

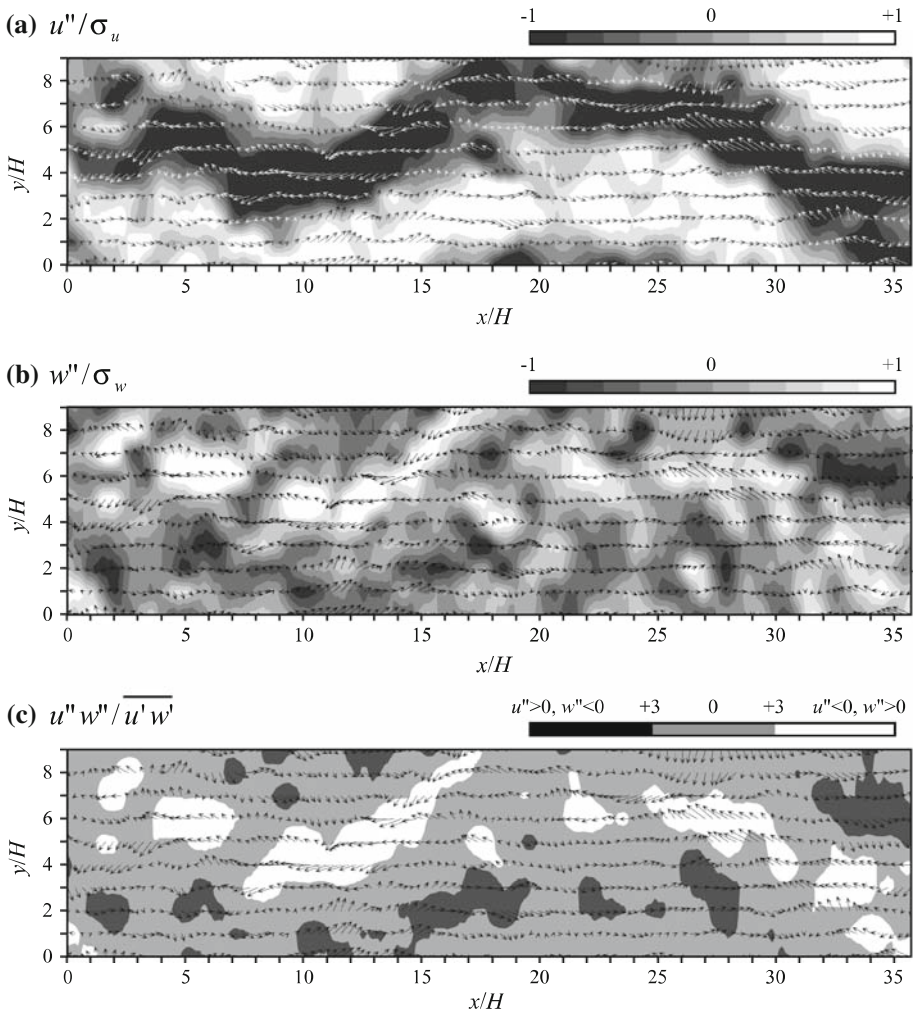

Fig. 9 Horizontal distributions of the velocity fluctuations filtered in the spanwise direction; (**a**) u''/σ_u, (**b**) w''/σ_w, and (**c**) $u''w''/\overline{u'w'}$. In (**c**), ejections occur in the white areas and sweeps occur in the black areas that have a magnitude three times larger than that of $\overline{u'w'}$

similarity as seen in Table 1, which is another perspective of Townsend's hypothesis of defining active motion, and also resulted in spatial filtering. Therefore, the streaky structures are considered to be a sequence of active motions.

5.3 Horizontal Vortices

The hairpin vortices play an important role in determining the characteristics of the packet structure and VLSM. Although it is difficult to capture the full 3D shapes of hairpin vortices experimentally, some vortex signatures should be available in one- or two-dimensional datasets. Tomkins and Adrian (2003) observed that pairs of counter-rotating vortices, which are

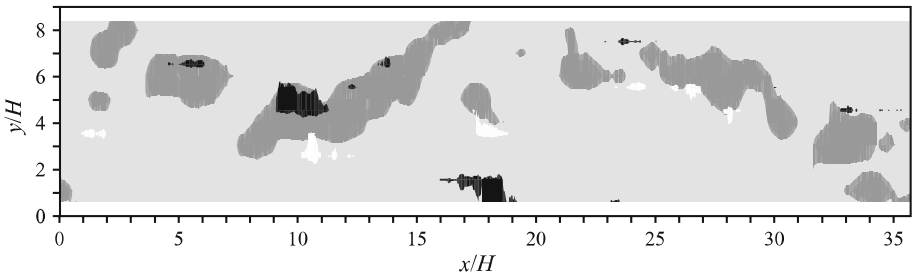

Fig. 10 Horizontal distributions of swirling strength $\lambda_{ci}(\omega_z/|\omega_z|)$ and ejection. The *white area* represents anticlockwise rotation and the *black area* represent clockwise rotation. *Dark grey area* represents the occurrence of ejection, using the same criteria as in Fig. 9c

considered to be the legs of the hairpin vortices, frequently occur in the left and right sides of very large streaks in a low-momentum fluid.

Figure 10 shows the locations of the swirling strength λ_{ci} plotted together with those of the ejections on the same horizontal slice as Fig. 9. The swirling strength is reliably used to identify the location of vortex cores (Zhou et al. 1999; Tomkins and Adrian 2003). In this figure, the swirling strength was multiplied by the sign of the vorticity $(\omega_z/|\omega_z|)$ to specify the direction of rotation, with a positive/negative value indicating the anticlockwise/clockwise rotation.

In COSMO, the swirling motions were frequently observed beside the locations of ejections. The identified swirling motions rotate clockwise if they are at the left side of the ejection, facing the streamwise direction, and vice versa. The symmetric counter-rotating motions are rare and most of the swirling motions are one-sided. These one-sided vortices are consistent with asymmetric hairpin vortices (Tomkins and Adrian 2003).

To clarify the relationship between the ejections and their surrounding vector fields more clearly, the horizontal vector fields were averaged, centering on the point where the prominent ejection occurred. The image composite technique is often used to visualize the average shape of coherent turbulence. Tomkins and Adrian (2003) averaged coherent turbulence centred about a point of the low velocity area to observe the vector fields surrounding the very large low-speed streak. Watanabe (2004) used a wavelet transform to detect the microfront in the scalar fluctuation for the centre of the image composite.

We focus the flow around the prominent ejection. In the horizontal field, we extracted the areas where the magnitude of the ejection was 'a' times larger than that of $-\overline{u'w'}$. The spatio-temporally coherent area that satisfied the above threshold was considered to be a coherent ejection. Within the coherent ejection, we found the point of maximum ejection to identify the centre of the composite image. The vector fields were averaged using the detected grid as the central point of reference. In this analysis, the choice of the threshold parameter 'a' was critical in determining the result, and we used $a = 4$, although the following results are still robust for any value in the range 1–5.

Figure 11 shows the contours of the composite u'' with horizontal velocity vectors. A pair of counter-rotating vortices is superimposed over the centre of the ejection. Although these symmetric motions might be due to the result of the ensemble averaging of one-sided vortices, which exist with even probability for both sides of the ejections as seen in Fig. 10, the relationship between the ejections and the horizontal vortices is shown to be robust. The similar ensemble-averaged structures are also observed over flat and smooth walls (Tomkins and Adrian 2003), and Coceal et al. (2007) confirmed such counter-rotating horizontal vortices

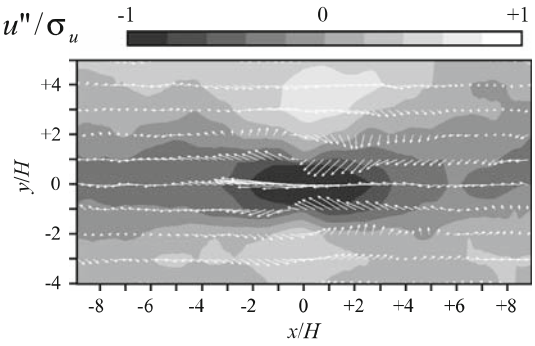

Fig. 11 Ensemble average of the fluctuation velocity vector fields around the prominent ejection events. The contour indicates the distribution of u''/σ_u

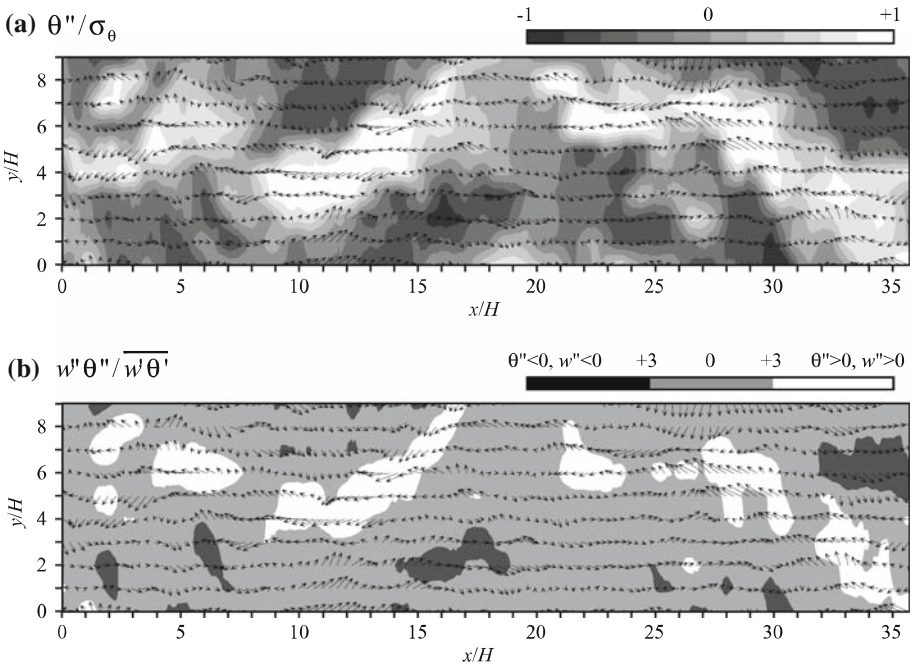

Fig. 12 Same as Fig. 9, but for (**a**) θ''/σ_θ and (**b**) $w''\theta''/\overline{w'\theta'}$

over an array of cubical obstacles using DNS. These results support the possibility of hairpin vortices within the logarithmic layer, irrespective of the surface configuration and the inactive motions.

5.4 Horizontal Distribution of the Temperature Fluctuations

Figure 12 shows the horizontal distributions of θ'' and $w''\theta''$ calculated using the filter in the spanwise direction at the same horizontal domain as in Fig. 9. Similar to Fig. 9c, the black and white parts of the distribution of $w''\theta''$ indicate the occurrences of positive $w''\theta''$, for a downdraft ($w'' < 0$ and $\theta'' < 0$) and for an updraft ($w'' > 0$ and $\theta'' > 0$). These were three times larger in magnitude than that of $\overline{w'\theta'}$. The distribution of θ'' in Fig. 12a corresponds closely to that of u'' in Fig. 9a. This is because the thermal stratification was near neutral

(slightly unstable) during this experimental period, and so, the updraft brought low speed and high temperature air upward, and the downdraft caused the opposite to occur. It should be noted that, for near-neutral conditions, the thermal stratification has negligible effects on the flow field at this measurement height. Therefore, this turbulent flow field was dominated by forced convection, and temperature behaved as a passive scalar.

It is interesting to note that the best correspondence with the structure of θ'' was not that of w'', but rather that of u''. In Fig. 12b, which shows the horizontal distribution of the vertical heat flux, with the black and white parts distinguished following the same criteria in Fig. 9c. The distribution of $w''\theta''$ corresponded closely to that of $u''w''$, as expected.

The exchange processes for heat and momentum at the surface do not correspond to each other (Kanda et al. 2007) because the form drag contributes only to the latter. However, such a difference would be merged at elevations up to $2H$ in COSMO, due to the strong mixing within the roughness sublayer, so that the vertical transport of momentum and heat would be similar within the inertial sublayer.

6 Concluding Remarks

We experimentally examined the coherent turbulent structures within very high Reynolds number atmospheric flow over very large roughness. The results support Townsend's Reynolds number similarity of the structure of wall turbulence with respect to the active motion. As observed in several experiments over different types of roughness, very large structures of low momentum elongated along the streamwise direction were observed in this experiment. Such structures account for the major part of the local Reynolds stress. Further discussions and experiments are necessary for the quantitative evaluation of their structural similarity so as to reveal the scaling parameter of the coherent structures and to understand the physical mechanism for the development of coherent turbulence.

In the COSMO experiment, the moving average along the spanwise direction was practically applicable to separate the active and inactive motions since their spanwise length scales are sufficiently different. This strategy does not ensure the applicability of the same method to other experiments because the characteristics of inactive motions is highly dependent on the experimental settings, e.g. buoyancy driven or topography induced convection in the ABL, artificial low frequency pressure fluctuations (Bradshaw 1967), and naturally induced low frequency motions above the outer layer of the canonical turbulent boundary layer. Although these are expected to be all inactive to the inner-layer motions, their shapes or scales are not consistent. Therefore, the types of filter functions, their sizes, and the direction of filtering to be applied for separating the active and inactive motions have to be selected appropriately for the experiment.

Finally, the observed coherent structure is expected to have a relevant influence on the ventilation mechanism of the canopy air mass in built-up areas, of a city. The ventilation process might be controlled, not only by the local environment such as the configurations of neighbouring buildings, but also by much larger scale motions developed above the canopy layer. Therefore, the characteristics of the coherent active motions have to be further investigated to also understand the scalar and momentum exchanges in cities.

Acknowledgements This research was financially supported by the Core Research for Evolution Science and Technology Program of the Japanese Science and Technology Cooperation and a grant-in-aid for JSPS fellows.

References

Adrian RJ, Meinhart CD, Tomkins CD (2000) Vortex organization in the outer region of the turbulent boundary layer. J Fluid Mech 422:1–54

Bhaganagar K, Kim J, Coleman G (2004) Effect of roughness on wall-bounded turbulence. Flow Turb Combust 72:463–492

Bradshaw P (1967) Inactive motions and pressure fluctuations in turbulent boundary layers. J Fluid Mech 30:241–258

Christen A, Gorsel E, Vogt R (2007) Coherent structures in urban roughness sublayer turbulence. Int J Climatol 27:1955–1968

Castro IP, Cheng H, Reynolds R (2006) Turbulence over urban-type roughness: deductions from wind-tunnel measurements. Boundary-Layer Meteorol 118:109–131

Coceal O, Dobre A, Thomas TG, Belcher SE (2007) Structure of turbulent flow over regular arrays of cubical roughness. J Fluid Mech 589:375–409

Dennis DJC, Nickels TB (2008) On the limitations of Taylor's hypothesis in constructing long structures in a turbulent boundary layer. J Fluid Mech 614:197–206

Drobinski P, Carlotti P, Newsom RK, Banta RM, Foster RC, Redelsperger JL (2004) The structure of the near-neutral atmospheric surface layer. J Atmos Sci 61:699–714

Foster RC, Vianey F, Drobinski P, Carlotti P (2006) Near-surface coherent structures and the vertical momentum flux in a large-eddy simulation of the neutrally-stratified boundary layer. Boundary-Layer Meteorol 120:229–255

Head MR, Bandyopadhyay P (1981) New aspects of turbulent boundary-layer structure. J Fluid Mech 107:297–337

Hutchins N, Marusic I (2007) Evidence of very long meandering features in the logarithmic region of turbulent boundary layers. J Fluid Mech 579:1–28

Inagaki A, Kanda M (2008) Turbulent flow similarity over an array of cubes in near-neutrally stratified atmospheric flow. J Fluid Mech 615:101–120

Kaimal JC, Wyngaard JC, Izumi Y, Cote OR (1972) Spectral characteristics of surface layer turbulence. Q J Roy Meteorol Soc 98:563–589

Kanda M, Moriwaki R, Kasamatsu F (2004) Large eddy simulation of turbulent organized structure within and above explicitly resolved cubic arrays. Boundary-Layer Meteorol 112:343–368

Kanda M (2006) Large eddy simulations on the effects of surface geometry of building arrays on turbulent organized structures. Boundary-Layer Meteorol 118:151–168

Kanda M, Kanega M, Kawai T, Sugawara H, Moriwaki R (2007) Roughness lengths for momentum and heat derived from outdoor urban scale models. J Appl Meteorol Climatol 46:1067–1079

Kawahara G, Kida S (2001) Periodic motion embedded in plane Couette turbulence: regeneration cycle and burst. J Fluid Mech 449:291–300

Kim KC, Adrian RJ (1999) Very large-scale motion in the outer layer. Phys Fluid 11:417–422

Klein SJ, Reynolds WC, Schraub FA, Runstadler PW (1967) The structure of turbulent boundary layers. J Fluid Mech 30:741–773

Krogstad P-A, Antonia RA, Browne WB (1992) Comparison between rough- and smooth-wall turbulent boundary layers. J Fluid Mech 245:599–617

Kunkel GJ, Marusic I (2006) Study of the near-wall-turbulent region of the high-Reynolds-number boundary layer using an atmospheric flow. J Fluid Mech 548:375–402

Lewalle J, Delville J, Bonnet JP (2000) Decomposition of mixing layer turbulence into coherent structure and background fluctuations. Flow Turb Combust 64:301–328

Marsic I, Hutchins N (2008) Study of the log-layer structure in wall turbulence over a very large range of Reynolds number. Flow Turb Combust 81:115–130

McNaughton KG, Raubach J (1998) Unsteadiness as a cause of non-equality of eddy diffusivities for heat and vapour at the base of an advective inversion. Boundary-Layer Meteorol 88:479–504

Moriwaki R, Kanda M (2006) Local and global similarity in turbulent transfer of heat, water vapor, and CO_2 in the dynamic convective sublayers over a suburban area. Boundary-Layer Meteorol 120:163–179

Newsom R, Calhoun R, Ligon D, Allwine J (2008) Linearly organized turbulence structures observed over a suburban area by dual-doppler lidar. Boundary-Layer Meteorol 127:111–130

Nickels TB, Marusic I, Hafez S, Chong MS (2005) Evidence of the k_1^{-1} Law in a high-Reynolds-number turbulent boundary layer. Phys Rev Lett 95:074501

Oikawa S, Meng Y (1995) Turbulence characteristics and organized motion in a suburban roughness sublayer. Boundary-Layer Meteorol 74:289–312

Porté-Agel F, Pahlow H, Meneveau C, Parlange MB (2001) Atmospheric stability effect on subgrid-scale physics for large-eddy simulation. Adv Water Res 24:1085–1102

Raupach MR, Antonia RA, Rajagopalan S (1991) Rough-wall turbulent boundary layers. Appl Mech Rev 44:1–25
Robinson SK (1991) Coherent motions in the turbulent boundary layer. Annu Rev Fluid Mech 32:519–571
Roth M (2000) Review of atmospheric turbulence over cities. Q J Roy Meteorol Soc 126:941–990
Shaw RH, Tavangar J, Ward DP (1983) Structure of Reynolds stress in a canopy layer. J Clim Appl Meteorol 22:1922–1931
Shaw RH, Brunet Y, Finnigan JJ, Raupach MR (1995) A wind tunnel study of air flow in waving wheat: two-point velocity statistics. Boundary-Layer Meteorol 76:349–376
Stull RB (1988) An introduction to boundary layer meteorology. Kluwer Academic Publishers, Dordrecht, 670 pp
Tomkins CJ, Adrian RJ (2003) Spanwise structure and scale growth in turbulent boundary layers. J Fluid Mech 490:37–74
Townsend AA (1976) The structure of turbulent shear flow. Cambridge University Press, Cambridge 429 pp
Volino RJ, Schultz MP, Flack KA (2007) Turbulent structure in rough- and smooth-wall boundary layers. J Fluid Mech 592:263–293
Watanabe T (2004) Large-eddy simulation of coherent turbulence structures associated with scalar ramps over plant canopies. Boundary-Layer Meteorol 112:307–341
Zhou J, Adrian RJ, Balachandar S, Kendall TM (1999) Mechanisms for generating coherent packets of hairpin vortices in channel flow. J Fluid Mech 387:353–396